# Microstructural and magnetic characterization of Fe- and Ir-based multilayers

E. Arias-Egido, M. A. Laguna-Marco, J. Sánchez-Marcos, C. Piquer, J. Chaboy, M. Ávila, and J. Garcia Lopez

Phys. Rev. Materials **2**, 014402 — Published 10 January 2018

DOI: 10.1103/PhysRevMaterials.2.014402

# Microstructural and magnetic characterization of Fe- and Ir-based multilayers

E. Arias-Egido,[1,2] M. A. Laguna-Marco,[1,2,*] J. Sánchez-Marcos,[3]
C. Piquer,[1,2] J. Chaboy,[2,4] M. Ávila,[5] and J. Garcia Lopez[6,7]

[1]*Instituto de Ciencia de Materiales de Aragón, CSIC - Universidad de Zaragoza, Zaragoza 50009, Spain*
[2]*Departamento de Física de la Materia Condensada, Universidad de Zaragoza, Zaragoza 50009, Spain*
[3]*Dep. Química-Física Aplicada, Universidad Autónoma de Madrid, Cantoblanco 28049, Madrid, Spain*
[4]*Diamond Light Source Ltd., Harwell Science and Innovation Campus, Chilton, Didcot, Oxfordshire, OX11 0DE, UK*
[5]*ALBA Synchrotron Light Source, Cerdanyola del Valls 08290, Barcelona, Spain*
[6]*Dpto. Física Atómica, Molecular y Nuclear, Universidad de Sevilla, Sevilla 41080, Spain*
[7]*CNA (U. Sevilla, J. Andalucia, CSIC), Av. Thomas A. Edison 7, Sevilla 41092, Spain*

(Dated: December 11, 2017)

Nominal $[\mathrm{Fe}(t)/\mathrm{Ir}(t')]_n$ (M/M type), $[\mathrm{FeOx}(t)/\mathrm{IrOx}(t')]_n$ (O/O) and $[\mathrm{Fe}(t)/\mathrm{IrOx}(t')]_n$ (M/O) multilayers have been prepared by magnetron sputtering at room temperature. Composition, structure and magnetic behavior have been analyzed. In the M/M samples, the Fe and Ir phases are identified as bcc and fcc, respectively. The magnetism evolves from bulk-like iron to granular behavior as the thickness of the Fe layers decreases. An induced magnetic moment, ferromagnetically coupled to Fe, is observed on Ir by XMCD. Besides, the presence of negative remanent magnetization is observed in the M/M samples. As for the M/O samples, the stronger affinity of iron for oxygen displaces the oxygen atoms giving rise to actual heterostructures that strongly differ from the nominal ones. For similar thickness of the two layers the Fe layer become oxidized while a mixture of metal and oxide phases is found in the Ir layer. The increase of the Fe thickness leads to a metallic Ir layer and a highly coercive ($\sim$ 4.4 kOe) core-shell metal-oxide structure in the Fe layers.

PACS numbers:

## I. INTRODUCTION

Binary thin films and heterostructures based on combinations of Fe and heavier metals such as Ag, W, Pt or Au have attracted wide attention for practical spintronic applications.[1–6]. Anomalous Hall effect and spin-dependent transport have been reported in Fe/Au multilayers[3,4] and a large number of works has been devoted to Fe/Pt multilayers for promising applications in spin electronics and ultrahigh-density magnetic information storage[7–10]. In the last few years the interest in Fe- and Pt-based multilayers has been extended to their oxides[11–13]. In all the cases the key ingredient is the high magnetocrystalline anisotropy, whose origin lies in the strong spin-orbit interaction of the heavy 5d atom.

Fe-Ir systems, on the other hand, have been barely explored. The few works reported so far are mostly devoted to the structural (strain) effects on ultrathin Fe layers by epitaxially growth on Ir substrates[14–16]. Regarding the magnetism, the majority of the works are theoretical and limited to the study of the magnetic arrangement in the first Fe monolayers of these epitaxially strained films.[17–19] The lack of investigation on Fe-Ir systems is surprising taking into account that Ir also exhibit a strong spin-orbit interaction[20] and is at the origin of the large magnetocristalline anisotropy of the commonly used bimetallic antiferromagnet MnIr[21]. In addition, the strong spin-orbit interaction of Ir has recently attracted renewed attention regarding iridium oxides, where a plethora of new phenomena and new spintronic materials has appeared.[22] Even the simplest iridate, $IrO_2$, has been recently proposed as the most promising material for spin-current detection.[23] Nevertheless, no iron oxide/iridium oxide system has been studied so far. Therefore, we propose to explore three different Fe and Ir heterostructures: (i) Fe metal/Ir metal, (ii) Fe oxide/Ir oxide and (iii) Fe metal/Ir oxide multilayers. The samples were prepared in favorable industrial production conditions, i.e. those conditions that are more interesting from the practical point of view: they were grown by conventional sequential magnetron sputtering at room temperature. In the first two cases, the deposited layers are expected to remain metal or oxide according to the growth conditions. The last type of samples, on the other hand, were designed to study whether the diverse affinity for oxygen displaces the oxygen atoms giving rise to different core-shell structures depending on the relative amount of chemical species.[24] In this work we disentangle the structural and compositional details of samples grown under these three different conditions and analyze the interplay between structure and magnetic behavior.

## II. EXPERIMENTAL

The layers were grown by conventional (or reactive) magnetron sputtering from 2-inch high-purity iridium and iron targets in a sequential way and using pure Ar atmosphere (or an $O_2$/Ar mixture gas $\sim$ 24% $O_2$-rich). According to the expected thickness, the number of bilayers and the type of atmosphere used to grow

the layers the thin films are labeled as $[Fe(t)/Ir(t')]_n$, $[FeOx(t)/IrOx(t')]_n$ and $[Fe(t)/IrOx(t')]_n$, where $t$ and $t'$ are the nominal thickness of the Fe and Ir layers (in nm), $n$ is the number of bilayers and $FeOx$ and $IrOx$ stand for layers grown in an oxygen-containing atmosphere. Thus, the samples can be classified within three groups regarding their nominal composition, namely: metallic-metallic (M/M), oxide-oxide (O/O) and metallic-oxide (M/O). All samples were grown on a Si(100) substrate at room temperature. The preparation started with the Ir (iridium oxide) layer and a last Ir (iridium oxide) layer was deposited on top. The base pressure provided by the vacuum system was in the 0.3-2 $\times$ $10^{-6}$ mbar range and the working pressure was $\sim 5 \times 10^{-3}$ mbar.

X-Ray Reflectivity (XRR) and X-ray diffraction measusements (XRD) were performed on a Bruker D8 X-ray diffractometer by using the $K_\alpha$ radiation line of copper. The multilayer structure was further characterized by transmission electron microscopy (TEM). TEM images were obtained at 200 kV with a JEOL 2000 FXII microscope, 0.28 nm point to point spatial resolution. Gatan Digital Micrograph program was used for image capture and analysis.

The study of the short-range crystal structure around both Fe and Ir centers as well as their electronic configuration was performed by X-ray absorption spectroscopy (XAS) at the Fe K edge and the Ir $L_3$ edge. Both regions of the XAS spectrum, the X-ray absorption near edge structure (XANES) and the extended X-ray absorption fine structure (EXAFS), were recorded. XAS spectra were measured in the fluorescence yield mode at CLAESS beamline of the ALBA synchrotron. Energy was set using a Si(111) double crystal monochromator. High order harmonics were rejected by selecting the Rh coating of both vertically collimating and focusing mirrors. The incoming beam was monitored by an $N_2$-filled ionization chamber and the fluorescence lines were detected using a Si-drift-detector. The *ab-initio* computation of the XANES spectra was carried out using the multiple-scattering code Continuum[25] included in the MXAN package[26]. A complete discussion of the followed procedure can be found elsewhere[27–29]. EXAFS spectra were analyzed according to standard procedures[30] using the HORAE-IFEFFIT (Athena, Artemis) program package and the FEFF code for the *ab-initio* multiple scattering EXAFS simulations.[31,32].

Rutherford Backscattering Spectrometry (RBS) experiments were carried out at the Centro Nacional de Aceleradores (Sevilla, Spain). A 1.514 MeV $He^{2+}$ beam and a 3.016 MeV $He^{2+}$, with beam diameter of $\sim$1mm and scattering angle of 110° were employed to determine the thickness of the samples in terms of at./cm$^2$ and the elemental composition of the multilayers.

Magnetic measurements were carried out in a SQUID magnetometer (MPMS-5, from Quantum Design). Magnetization hysteresis loops were achieved up to 50 kOe at room temperature and 5 K after cooling the samples under an applied field of 10 kOe. Magnetization versus temperature data were collected from 5 to 350 K with a heating rate of 5 K/min at 100 and 1000 Oe.

XMCD measurements were carried out at the 4-ID-D beamline of the Advanced Photon Source at Argonne National Laboratory. Fluorescence XMCD spectra were recorded at the Ir $L_2$ and $L_3$ edges at 10 K for the two directions of the applied magnetic field (3.5 T), along and opposite to the incident photon wavevector, to remove spurious signals. Undulator radiation was monochromatized with double Si(111) crystals and its polarization converted from linear to circular with a diamond quarter-wave plate operated in Bragg transmission geometry.

$^{57}$Fe Mössbauer spectroscopy was carried out in emission mode (CEMS). The spectra were recorded at room temperature in triangle mode, using a conventional Mössbauer spectrometer with $^{57}$Co(Rh) source. Spectra were analyzed by a non-linear fit using the NORMOS program[33]. Isomer shifts were referred to the $\alpha$-Fe used for energy calibration. Samples were placed in an He4%$CH_4$ gas flow proportional counter to detect the internal conversion electrons emitted by the Fe nuclei after resonant absorption of gamma rays.

## III. RESULTS AND DISCUSSION

### A. Structural Characterization

The multilayer structure was probed by means of XRR and TEM. The corresponding bilayer thickness calculated from XRR and the values of the thickness of each layer measured on the TEM images are shown in table I. Cross-sectional TEM images of the samples are shown in Fig. 1. Clear layered structures can be observed in all the samples, even in those with a large number (50) of very thin (1-2 nm) layers. As expected, the roughness of the layers is higher for samples grown under an $O_2$/Ar mixture atmosphere and also increases with the number of bilayers. Small regions of different shades of gray can be discerned inside each layer, which can be due to different crystal orientation and/or different phases within the layer. For example, the sharp contrast observed inside the Ir layer in sample $[Fe(10)/Ir(10)]_{10}$ (panel (b) of Fig. 1) suggests different grain orientation, whereas the *clusters* observed inside the Fe layer of sample $[Fe(5)/IrOx(2)]_{20}$ (panel (d)) look similar to a cluster/matrix biphasic system. Moreover, the presence of some crystalline planes, observable in most of the samples in Fig. 1 proves the existence of certain degree of crystallinity (polycrystallinity). On the other hand, on sample $[FeOx(2)/IrOx(2)]_{50}$ no crystalline planes can be distinguished, which suggests higher degree of disorder due to the smaller size of the layer. Additional details are displayed in the Supplemental Material (SM)[34].

No diffraction peaks were detected in the XRD patterns (not shown), likely due to the smallness of the samples along with their polycrystalline character and short-range crystallographic order.

TABLE I: Bilayer thickness calculated from XRR data and individual layer thickness according to TEM (both in nm, ±0.5nm); total multilayer thickness (in $10^{15}$ at/cm$^2$) and relative abundance of elements obtained from RBS.

| Sample | XRR | TEM | Atoms | Composition |
|---|---|---|---|---|
| $[Fe(2)/Ir(2)]_{20}$ | 3.2 | 1.2/1.8 | 460 | Ir47Fe51Ar2 |
| $[Fe(10)/Ir(10)]_{10}$ | 16.1 | 6.7/9.0 | 1050 | Ir52Fe48Ar0 |
| $[FeOx(2)/IrOx(2)]_{50}$ | 4.0 | 1.0/1.9 | 1780 | Ir17Fe13O69Ar1 |
| $[Fe(2)/IrOx(2)]_{50}$ | 3.9 | 1.8/1.5 | 1620 | Ir16Fe30O53Ar1 |
| $[Fe(5)/IrOx(2)]_{20}$ | 6.9 | 4.5/1.7 | 1150 | Ir10Fe44O44Ar2 |

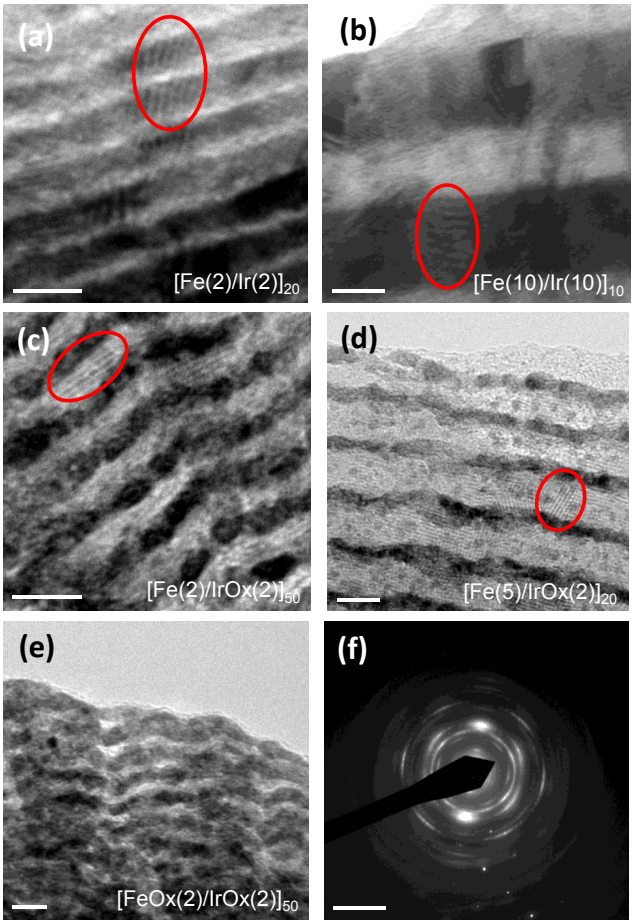


FIG. 1: TEM images of the M/M (top), M/O (middle) and O/O (bottom) samples showing layered structure with darker Ir-containing and lighter Fe-containing layers. The panel (f) shows the FT corresponding to the $[Fe(5)/IrOx(2)]_{20}$ sample.

The XAS spectrum recorded at the Fe K edge for a M/M sample ($[Fe(2)/Ir(2)]_{20}$) is shown in Fig. 2. The comparison with the references shows that the sample is fully metallic as expected. However, the details of the profile, i.e. the position and width of the features, do not match the profile of the references: bulk bcc Fe, bulk fcc Ni or fcc-Fe nanoparticles[5,35]. For instance, in the 7120-7145 eV range, the three references display two features, whereas only one peak is observed in our multilayer.

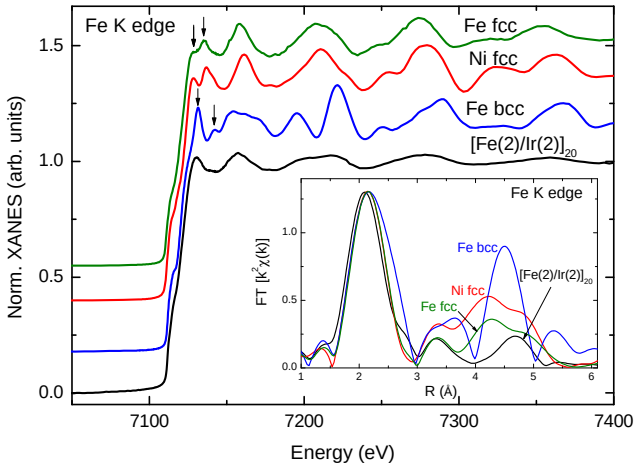


FIG. 2: Fe K-edge XAS spectra recorded on $[Fe(2)/Ir(2)]_{20}$ and bulk Fe, bulk Ni and fcc-Fe NPs[35] references. The inset shows the modulus of the Fourier transforms of the $k^2$-weighted EXAFS signals in the range from 3 Å$^{-1}$ to 10 Å$^{-1}$. For the sake of a better comparison the FT of the references has been multiplied by a factor of 0.3.

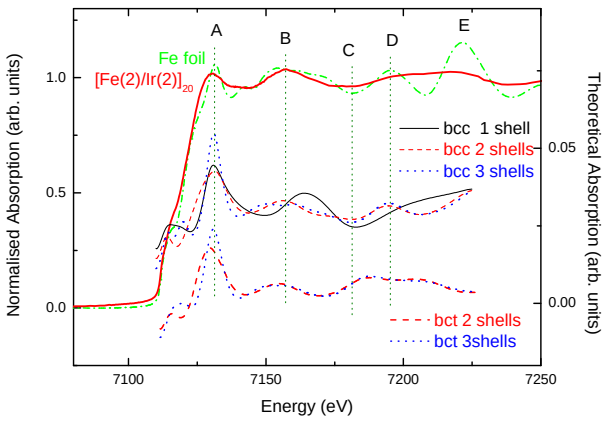


FIG. 3: The Fe K-edge XANES spectra recorded on the $[Fe(2)/Ir(2)]_{20}$ sample is compared to the theoretical spectra obtained for Fe bcc clusters.

The FT of the EXAFS spectra is shown in the inset of Fig. 2 (all the recorded EXAFS are included in the SM). The FT profile at higher R reveals a bcc-like symmetry and the intensity decrease relative to the bulk references indicates structural disorder. The disordered bcc crystal structure of Fe has been further confirmed by thorough simulations of both XANES and EXAFS regions. In this way, the features of the XANES spectrum of the $[Fe(2)/Ir(2)]_{20}$ sample are well reproduced with two coordination shells with bcc structure, as can be seen in Fig. 3. For the sake of readability the complete computation analysis has been included in the SM. All to-

gether, the XAS analysis indicates that the iron layer of the $[Fe(2)/Ir(2)]_{20}$ sample can be accounted for in terms of a disordered bcc structure and discards the formation of disordered fcc or bct structures. It is worth noticing at this point that the degree of disorder may not be homogeneous but variable through the iron layer. In this respect, similar FTs have been reported for FeAg granular alloys and ascribed to the presence of Fe in both crystalline and amorphous regions.[6]

Fig. 4 shows the absorption spectrum recorded on the O/O sample. An oxidation state of 2.85+ can be estimated from the position of the threshold. The poor structure of the XANES spectrum indicates a highly disordered local structure around Fe in this sample. In fact, the XANES profile of our sample seems less structured than that of ferryhydrite, typically considered a structurally disordered iron oxide itself, while resembles that found on very short-range coordinated Fe-O arrangements such as mesoporous aluminosilicates with a tiny 0.5 wt% load of iron and simple $Fe^{3+}$ aqueous solutions[36,37] (see inset of Fig. 4).

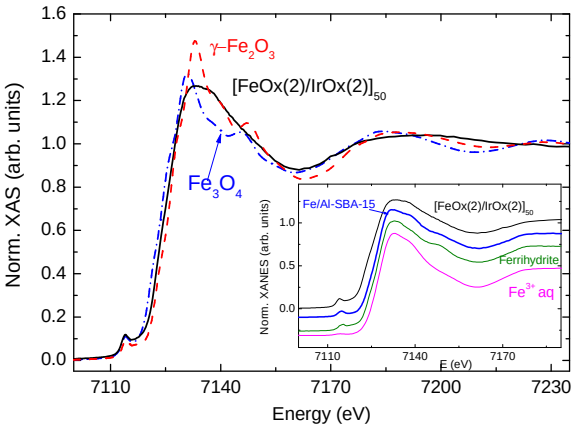


FIG. 4: Fe K-edge XAS spectra recorded on $[FeOx(2)/IrOx(2)]_{50}$ and bulk $Fe_2O_3$ and $Fe_3O_4$ references. The inset shows the comparison to ferrihydrite, a mesoporous aluminosilicate with 0.5 wt% of Fe and a simple $Fe^{3+}$ aqueous solution.

As for the (nominally) M/O samples, the XANES spectra and the FT of the EXAFS spectra are displayed in Fig. 5 and Fig. 6, respectively. In the $[Fe(5)/IrOx(2)]_{20}$ sample, both the XANES and the FT indicate a mixture of metal and oxide phases even when, according to the growth conditions, the Fe-based layer should be Fe metal. In particular, in the XANES spectra the energy position of the threshold, the height of the pre-edge at $\sim 7115$ eV and the profile just above the edge can only be accounted for by an addition of metal Fe and iron oxide. In the FT, the peak at $\sim 2$ Å in the real part reveals a metallic contribution added to the main oxide phase. The linear combination fit of the XANES profile estimates that $\sim 60\%$ of the Fe atoms are in an oxide phase. It is worth noticing that the same rough estimation is obtained here regard-

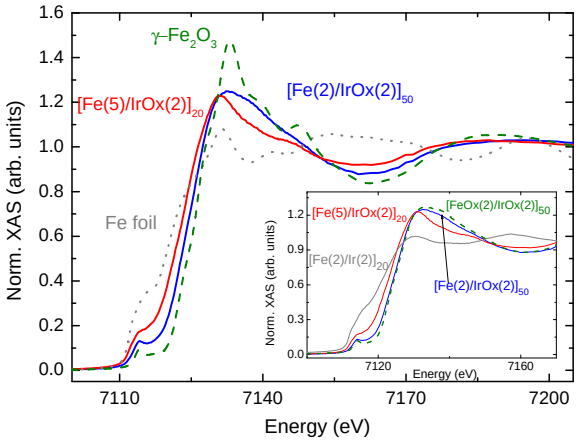


FIG. 5: Fe K-edge XAS spectra of $[Fe(2)/IrOx(2)]_{50}$, $[Fe(5)/IrOx(2)]_{20}$ and bulk $Fe_2O_3$ and Fe foil references.

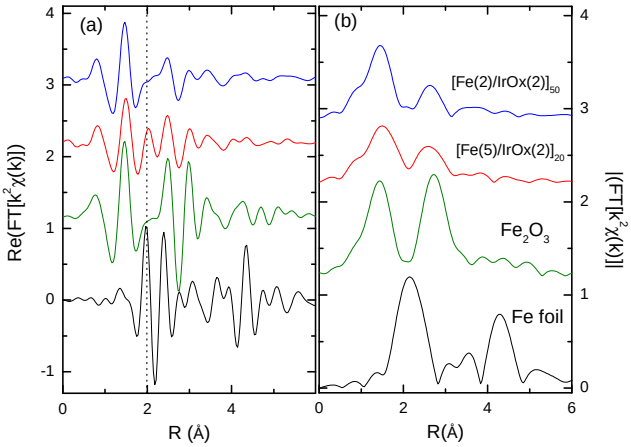


FIG. 6: Fourier transforms ((a) real part, (b) modulus) of the $k^2$-weighted Fe K-edge EXAFS signal in the range from 3 $Å^{-1}$ to 10 $Å^{-1}$. The doted line is a guide for the eye.

less of the chosen references: maghemite and Fe foil or $[Fe(2)/Ir(2)]_{20}$ and $[FeOx(2)/IrOx(2)]_{50}$. In relation to the degree of crystallinity, Fig. 6 shows the presence of a second peak at R $\sim 2.7$ Å on the FT, clearly indicating the formation of a second coordination shell in the oxide. However, the reduced intensity of the peaks in the FT relative to the bulk references and the fact that this reduction is larger for the second peak indicates certain degree of crystallographic disorder. This disorder, along with the presence of two phases, prevents the oxide in the Fe layer from being identified as a specific crystallographic phase. The same conclusions can be drawn for the (nominally) $[Fe(2)/IrOx(2)]_n$ sample: there is a mixture of metal and oxide phases, both of them structurally disordered. From the linear combination fit analysis at both regions, EXAFS and XANES, we get a $\sim 90$ % of the Fe atoms in an oxide phase.

Next, in order to probe the structure and composition

of the Ir-based layer the absorption spectra were recorded at the Ir $L_3$ edge (Fig. 7). Sample $[Fe(2)/Ir(2)]_{20}$ shows the expected XANES profile for metallic fcc Ir[38]. Similarly, sample $[FeOx(2)/IrOx(2)]_{50}$ shows the profile expected for $IrO_2$.[38] M/O Samples show an intermediate profile. Applying a linear combination fit analysis the amount of Ir atoms in the oxide phase has been estimated: $\sim$ 5% in $[Fe(5)/IrOx(2)]_{20}$, and $\sim$ 45% in $[Fe(2)/IrOx(2)]_{50}$.

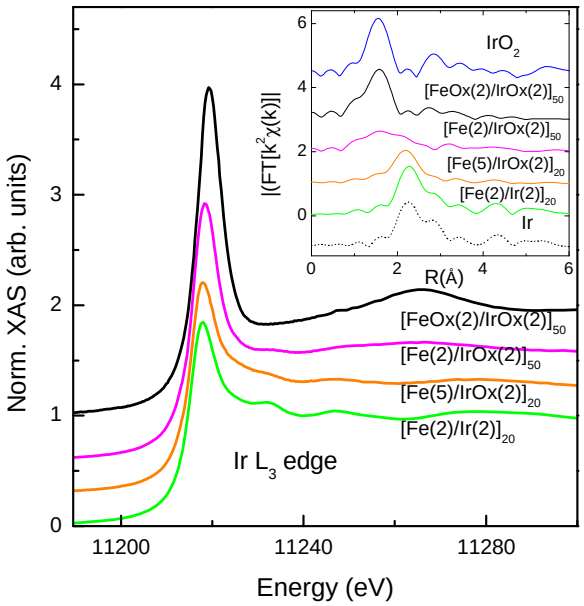


FIG. 7: Comparison of the Ir $L_3$-edge XANES spectra. For the sake of clarity the spectra have been vertically shifted. (inset) Fourier transforms ($k^2$-weighted, range from 3.1 $Å^{-1}$ to 10 $Å^{-1}$) of the EXAFS signals recorded at the Ir $L_3$ edge. The dotted line corresponds to the simulated spectrum of Ir metal. $IrO_2$ was measured in transmission geometry.

The EXAFS results are in agreement with the analysis of the XANES region. The FTs in the inset of Fig. 7 reveal that the Ir layer in $[Fe(2)/Ir(2)]_{20}$ corresponds to Ir metal. Due to the lack of an experimental reference, a simulated spectrum of Ir metal has been used for comparison (details in the SM). It can be also concluded that the Ir layers present a remarkable structural order taking into account that the thickness is only 2 nm. In the case of the O/O sample, its FT matches well with that of $IrO_2$. As for the M/O samples, the profile of sample $[Fe(5)/IrOx(2)]_{20}$ corresponds to Ir metal, even when it was grown as iridium oxide. In sample $[Fe(2)/IrOx(2)]_{20}$ the FT data indicate a significant contribution of both metallic and oxide phases. A rough estimation, using $[Fe(2)/Ir(2)]_{20}$ and $[FeOx(2)/IrOx(2)]_{50}$ as references, indicates that $\sim$ 60% of Ir atoms are in the oxide phase.

### B. Magnetic Characterization

Fig. 8 and Fig. 9 show the magnetization as a function of the applied field and the temperature, respectively.

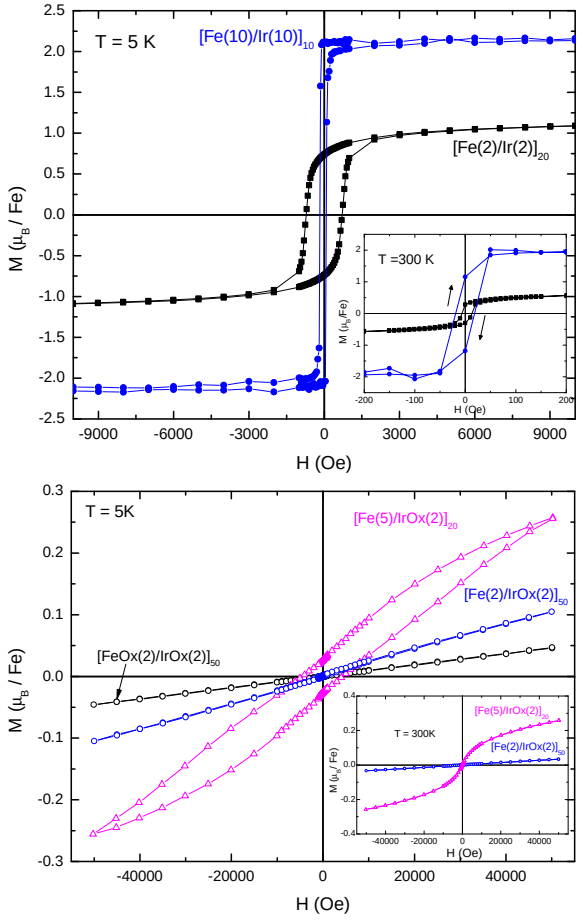


FIG. 8: Magnetic isotherms recorded at T = 5 K after field cooling. The insets show the magnetic isotherms recorded at T = 300 K

Sample $[Fe(10)/Ir(10)]_{10}$ shows a squared hysteresis loop with a magnetic moment of 2.16 $\mu_B$/Fe and very low coercivity. Besides, both, FC and ZFC, M(T) curves are nearly constant in the whole temperature range. Therefore, our data show that 10 nm of thickness is enough to show a behavior similar to that found in bulk Fe bcc (i.e. a system where the magnetic interaction is percolated along the whole layer). As the thickness of the Fe layer in M/M samples decreases the profile of the hysteresis loop becomes less squared, the magnetic moment decreases down to 1.20 $\mu_B$/Fe and the coercivity at low temperature increases from 125 Oe up to 700 Oe. In the M(T) curves the separation between the FC and ZFC branches at low temperature (irreversibility) increases and the FC M(T) curve becomes less flat. Sample $[Fe(2)/Ir(2)]_{20}$ presents a $\sim$ 60% reduction of the magnetization. This indicates an evolution from a magnetically percolated system (i.e. strongly interacting grains)

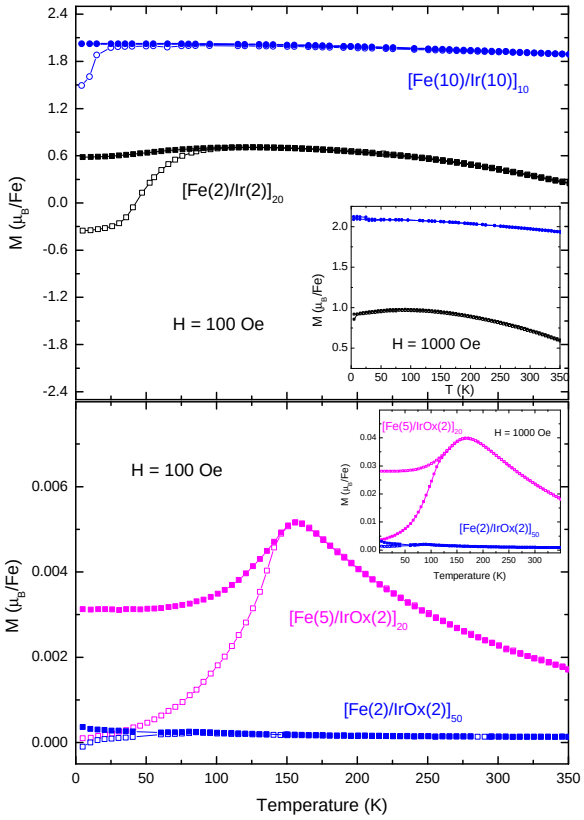


FIG. 9: FC and ZFC magnetothermal curves.

towards a weakly interacting granular system with decreasing Fe thickness.[39] The granular structure can be associated to better crystallized bcc magnetic regions (*clusters*) separated by more disordered regions (*matrix*) that inhibit the magnetic percolation. As discussed in the structural section, the reduction of the thickness is expected to reduce the grain size and increase the disorder. In addition, the decrease of the FC M(T) curve at low temperature suggests the presence of magnetically frustrated interactions between the clusters arising from the disorder and a re-entrant cluster glass (RCG) behaviour.

No exchange-bias is found in the M/M samples. On the other hand, they show exotic negative remanent magnetization (NRM) at RT and $[Fe(2)/Ir(2)]_{20}$ presents a negative value of the ZFC M(T) curve at low temperatures and low applied magnetic fields. NRM has been already reported in other nanostructured materials and molecular magnets[40–44]. The origin of this behaviour is yet under debate, but in most cases it is associated to the presence of two phases with differentiated magnetic response (magnetization and coercivity). In our compounds the NRM can be tentatively associated to the presence of a bimodal magnetization state formed by better defined FM bcc regions (seen as FM magnetic clusters) and crystallographically more disordered regions (seen as matrix between the clusters). Two different scenarios can be envisaged, (i) a scenario where the matrix is magnetically passive and behaves as RKKY medium between FM clusters favoring AFM alignment and (ii) a scenario where the matrix has magnetization and anisotropy different from those of the clusters. In this respect it should be recalled that according to the Bethe-Slater curve the interaction between iron atoms is FM in the bcc structure but AFM in the fcc one. The structural disorder and/or the presence of Ir near the interfaces can promote the appearance of AFM interactions.

The O/O multilayer shows a linear M(H) response with a small magnetic moment, below 0.1 $\mu_B$/Fe at H = 5 T (see bottom panel of Fig. 8). This linear M(H) behaviour discards the formation of maghemite-like phases, that should display hysteresis loops with a sizable magnetic moment. On the other hand, this behavior indicates a mainly paramagnetic (PM) behaviour. In addition, taking into account that most of the disordered iron oxides, such as goethite or ferrihydrite, are AFM in the bulk form and the antiferromagnetic nature of the superexchange interaction between iron atoms in all the iron oxides, the random formation of small regions with AFM or frustrated behavior cannot be ruled out.

The M(H) response of the M/O samples can be accounted for in terms of a system consisting of metallic magnetic Fe clusters in an oxidized matrix. The value of the magnetization depends on the fraction of Fe atoms in the metallic phase. Thus, according to XAS data, the Fe layer in the $[Fe(2)/IrOx(2)]_{50}$ sample is (almost) fully oxidized, resulting in a very small magnetization ($\sim$ 0.05 $\mu_B$/Fe at T = 5 K) and a M(H) response close to that found for the O/O samples. On the other hand, in the $[Fe(5)/IrOx(2)]_{20}$ sample, the oxygen initially in the Ir layer is not enough to fully oxidize the Fe layer so a significant part of the layer remains metallic and the magnetic moment rises up to $\sim$ 0.25 $\mu_B$/Fe for sample $[Fe(5)/IrOx(2)]_{20}$ at T = 5 K. At RT the M(H) shows the typical behavior of a superparamagnetic (SPM) system, but at low temperature the coercivity is high, $\sim$ 4400 Oe, a value that is among the highest reported for Fe-based systems.[24,45–47] Notwithstanding the high coercivity no exchange-bias is observed.

The thermal dependence (Fig. 9) also reflects the existence of magnetic clusters. The presence of $M_{max}$ (maximum value of the magnetization) and $T_{max}$ (temperature at which M reaches the maximum) is barely observable in $[Fe(2)/IrOx(2)]_{50}$ while both, $M_{max}$ and $T_{max}$, are much higher on $[Fe(5)/IrOx(2)]_{20}$, in agreement with the larger clusters size. In addition, the decrease of the FC curve as the temperature decreases at low temperatures indicates magnetically frustrated interacctions, i.e. the system does not behave as a SPM but as a cluster spin glass CSG (or super spin glass SSG).[48,49]

The Mössbauer spectra of representative samples are displayed in Fig. 10. None of them is magnetically split reflecting PM or SPM behavior at RT. The corresponding hyperfine parameters isomer shift, $\delta$, quadrupole split-

ting, $\Delta E_Q$, and linewitdth, $\Gamma$, are displayed in table II.

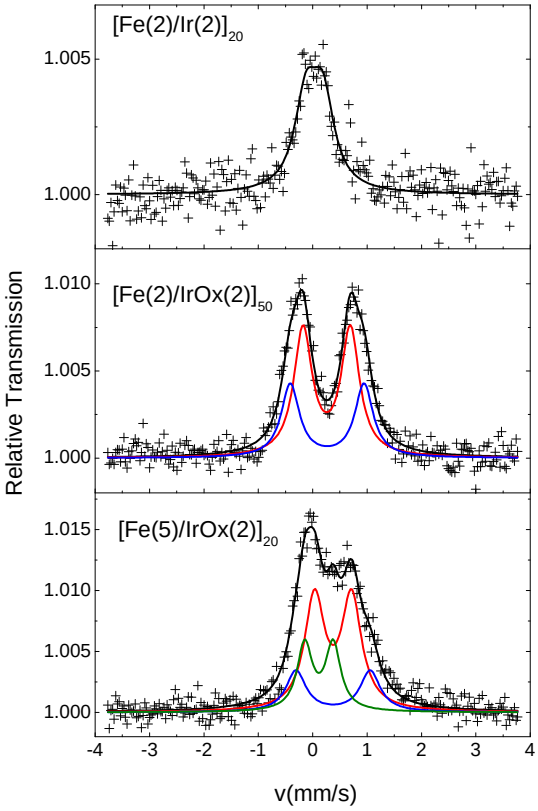


FIG. 10: Mössbauer spectra measured at room temperature. Each panel shows the experimental spectra (+), the overall fit (solid black lines), and the different components: 1 (red), 2 (blue) and 3 (olive) used to fit the experimental spectra.

In the $[Fe(2)/Ir(2)]_{20}$ sample, the poorly structured spectral profile and the high values of $\Delta E_Q$ indicate a metallic disordered environment. The high values of $\delta$ reflect the influence of the Ir atoms in the s density around the absorber. The existence of fcc Fe can be disregarded from the Mössbauer spectrum, since it would result in a negative isomer shift of ∼-0.09 mm/s.[50] The singlet measured at RT can be explained by the existence of a supermagnetic state at RT and further reinforces the model consisting on better crystallized bcc magnetic regions or clusters embedded in a more disordered Fe matrix.

The Mössbauer spectrum of $[Fe(2)/IrOx(2)]_{50}$ consist of a symmetric doublet that is best fitted with two symmetric doublets. Similar RT Mössbauer spectra with comparable hyperfine parameters have been found in different superparamagnetic antiferromagnetic $Fe^{3+}$ oxide nanoparticles such as goethite, hematite, ferrihydrite or magnetoferritin[51]. On the other hand, the Mössbauer profiles reported for nanoparticles of ferromagnetic Fe oxides (maghemite, magnetite) are not so similar to those obtained here.[52] Therefore, the Mössbauer spectrum indicates an (almost) fully oxide Fe layer, in consonance with XAS and magnetization data. Besides,

TABLE II: Mössbauer hyperfine parameters. In all cases the isomer shift is taken relative to $\alpha$-iron at 295 K.

| Sample | Intensity (%) | $\delta$ (mm/s) ±0.01 | $\Delta E_Q$ (mm/s) ±0.05 | $\Gamma$ (mm/s) ±0.05 |
|---|---|---|---|---|
| $[Fe(2)/Ir(2)]_{20}$ | 100 | 0.141 | 0.312 | 0.50 |
| $[Fe(2)/IrOx(2)]_{50}$ | 64 | 0.367 | 0.869 | 0.49 |
| | 36 | 0.376 | 1.356 | 0.40 |
| $[Fe(5)/IrOx(2)]_{20}$ | 55 | 0.483 | 0.678 | 0.44 |
| | 20 | 0.483 | 1.371 | 0.44 |
| | 25 | 0.224 | 0.521 | 0.33 |

this result points to the formation of a highly disordered AFM-like oxide. On the other hand, the spectrum of $[Fe(5)/IrOx(2)]_{20}$ consists on an asymmetric doublet and three symmetric doublets are needed to obtain a reasonable fit of the experimental data. This indicates that compared to $[Fe(2)/IrOx(2)]_{50}$, more environments with significant contribution exist in $[Fe(5)/IrOx(2)]_{20}$. By comparison, the two first components in the table can be assigned to the atoms of the oxidized regions and the third component, with lower $\delta$ and $\Delta E_Q$, can be assigned to the metallic atoms in the clusters. The Mössbauer results, therefore, also indicate a cluster spin glass system formed by metallic Fe clusters in an oxidized matrix.

XMCD spectra were recorded at the Ir $L_{2,3}$ edges to disentangle the presence of magnetization on the Ir layer (Fig. 11). Clear XMCD signals can be seen only for the $[Fe(2)/Ir(2)]_{20}$ and $[Fe(5)/IrOx(2)]_{10}$ samples. By contrast, in $[Fe(2)/IrOx(2)]_{20}$ the presence of XMCD is ambiguous. The XMCD spectral profile of $[Fe(2)/Ir(2)]_{20}$ resembles those reported for $Fe_{100-x}Ir_x$ intermetallic compounds[53]. Since Ir metal is not magnetic, this XMCD corresponds to the magnetic moment induced by Fe. The net magnetic moment derived from sum-rule analysis[54,55] ($m_l = 0.000\ \mu_B$/Ir, $m_s = 0.0015\ \mu_B$/Ir) indicates a spin nature and a ferromagnetic coupling to Fe. The FM coupling is in agreement with the results observed in bulk intermetallics and the calculations by Campbell[53,56]. The values of the moment, on the other hand, are one order of magnitude smaller than those found in Fe-Ir alloys[53]. This can be explained by the fact that only the Ir at the interface is expected to have a significant induced moment. Besides, we have seen that the magnetic moment in the $[Fe(2)/Ir(2)]_{20}$ sample is reduced relative to the bulk value (Fig. 8). This reduction of the Fe moment will in turn result in a smaller induced moment on Ir.

The XMCD spectra of the M/O samples show evident differences. The XMCD of $[Fe(5)/IrOx(2)]_{10}$ is clear and resembles that of the M/M sample. The net magnetic moment is also similar ($m_l = 0.004\ \mu_B$/Ir, $m_s = 0.0019\ \mu_B$/Ir). Therefore, this XMCD can be associated to the presence of metallic Fe/metallic Ir inter-

faces. On the other hand, when the Fe layer is 2 nm thick no clear XMCD can be observed. Since, according to XAS and magnetization data, the Fe layer is almost fully oxidized and not magnetic, no induced magnetism is expected in the Ir layer in this case. It is worth noticing, however, that this XMCD profile resembles those recorded in $Sr_2FeIrO_6$ and $Sr_2CoIrO_6$ samples.[57,58] The smallness of the signal does not allow an unmistakable analysis, but the presence of a small but real XMCD cannot be completely ruled out.

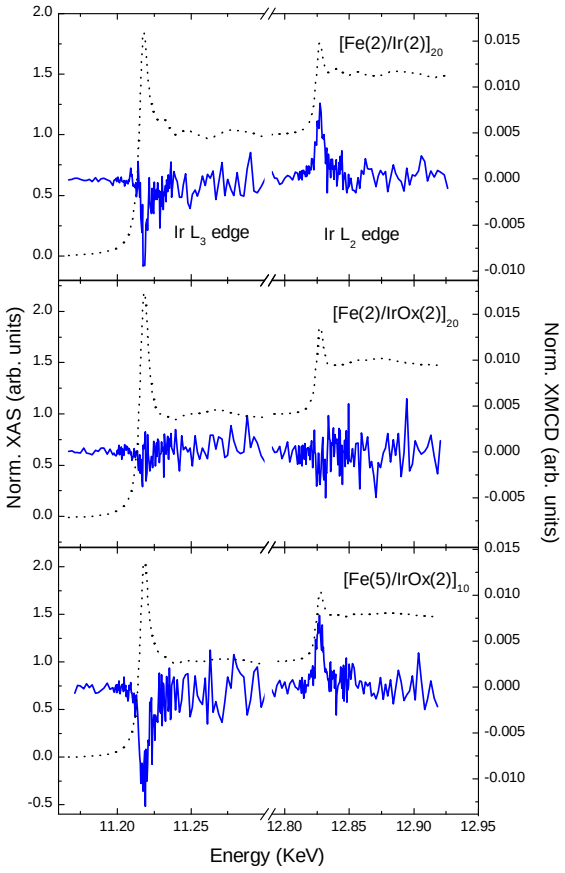


FIG. 11: Normalized XAS and XMCD spectra recorded at the $L_{2,3}$ edges of Ir at T = 10 K and H = 3.5 T on three representative samples.

Finally, the effect of annealing has been analyzed. Given the high coercivity, up to 63 KOe[59], reported for Fe/Pt thin films grown with substrate heating or with a post-annealing temperature treatment, the effect of thermal treatment has been explored in the Fe/Ir multilayers. The XRR data indicate a severe intermixing between layers while the magnetic data indicate a magnetization reduction and an slight increase of the coercivity up to 1.5 KOe, very far from those in Fe/Pt multilayers (see SM). This can be associated to the fact the Fe and Ir may only form a disordered fcc (A1) or disordered hcp (A3) phase, in contrast to the ordered $L1_0$ phase in Fe/Pt multilayers.

Regarding the O/O samples, the iron oxide phase may be identified as a disordered hematite. Application of standard thermal treatments to convert hematite into maghemite or magnetite to our multilayers causes also the reduction of the iridium oxide layer to Ir metal, showing that the thermal annealing is not a good way for the fabrication of well crystallized $[Fe_3O_4/IrO_2]_n$ or $[\gamma\text{-}Fe_2O_3/IrO_2]_n$ samples. Given their vast potential on spintronics,[11–13,23] alternative routes should be explored.

## IV. SUMMARY AND CONCLUSIONS

Nominal iron–iridium, iron–iridium oxide and iron oxide–iridium oxide multilayers have been prepared by sequential deposition of iron and iridium targets. Composition, structure and magnetic behavior have been analyzed by different techniques including TEM microscopy, RBS, XRR, XAS and Mössbauer spectroscopies and SQUID and XMCD magnetometries. Clear layered structures are found in all the samples. Both structure and magnetic behavior are found to be highly dependent on the preparation method conditions. In particular, three cases can be distinguished: M/M, M/O and O/O samples.

In the M/M samples, the Fe and Ir phases are identified as bcc and fcc structure, respectively. Despite the structural disorder in the Fe-based layer, the bcc structure is identified even for the thinnest $[Fe(2)/Ir(2)]_{20}$ sample. The formation of an Fe fcc structure induced by the fcc Ir substrate can be discarded. Similarly, no strained bct structure is found here, contrary to the situation found for MBE-grown samples[14,16]. The magnetic response is that expected for percolated thin films when the thickness of the Fe layer is $\sim$ 10nm. The thickness decrease results in a granular-like behavior. The granular system is weakly interacting but the slight decrease of the FC curves at low temperature suggests a RCG behavior. Besides, as the thickness decreases the relative weight of the disordered region (matrix) increases leading to an increase of the coercivity up to 700 Oe. The presence of induced Ir magnetic moments at the interface, ferromagnetically aligned to Fe as reveal by XMCD, may also contribute to the increase of the coercivity. Finally, the appearance of NRM rises the question of the possible role of Ir in this phenomenon, either promoting Fe-Fe distances with favorable AFM alignment in a similar way to that reported for Fe-Rh systems[60] or providing higher anisotropy to the Fe atoms at the interface.[7,21,61] While this question remains open, we believe our results will motivate further research since the NRM opens new possibilities in the design of new magnetic devices, as it allows the switching between two well differentiated magnetic states by applying very small magnetic fields.

In the O/O samples, the Ir phase has been identified as $IrO_2$. In the iron layer our results indicate a highly disordered oxide phase with only one coordination shell and an oxidation state close to $Fe^{3+}$. The magnetization

and Mössbauer measurements undoubtedly discard the formation of a ferro- or ferrimagnetic phase and indicate a PM behavior, which seems in accordance with an ill-defined iron oxide phase.

As for the M/O samples our work shows that the different affinity of Ir and Fe for oxygen is able to displace the oxygen from the iridium layer and form diverse metal-oxide structures depending on the Ir/Fe ratio. In this work, in the $[Fe(2)/IrOx(2)]_n$ sample, the oxygen initially in the Ir layer is enough to (almost) fully oxidize the Fe layer. The resulting Fe-based layer consists of very small metallic Fe clusters in a main Fe oxide matrix. At the same time, a biphase structure, metal and oxide, is formed in the Ir layer. For thicker Fe layers the oxygen is not enough to fully oxidize the Fe layer. In this case the Ir become purely metallic while the biphasic iron layer consists of large metallic clusters surrounded by an oxide matrix. The fractions of metal and oxide phases found by the different techniques (XAS, Mössbauer, magnetization and the compositional results found by RBS) show a remarkable agreement.

The magnetic data indicate large coercivity and a negligible exchange-bias. Besides, the M/O systems present a CSG behavior where the size of the metallic clusters and their magnetic response ($M_{max}$ and $T_{max}$) depends on the initial thickness ratios. Therefore, our work shows that the oxygen diffusion process can be used to obtain samples with tuned magnetic response. Finally, the XMCD spectra show that a magnetic moment is clearly induced in iridium for those samples with a metal-Fe/metal-Ir interface. On the other hand, further work is needed to clarify the origin of the XMCD at the $[Fe(2)/IrOx(2)]_n$ samples and the role of Ir in the high coercivity values.

### Acknowledgments

This work was partially supported by the Spanish Ministry of Economy and Competitiveness (MINECO) under contract project MAT2014-54425-R and by the Aragón DGA NETOSHIMA grant. E.A-E acknowledges the Spanish MINECO and the European Social Fund for a FPI (2015) grant. This research used resources of the APS, a U.S. Department of Energy (DOE) Office of Science User Facility operated for the DOE Office of Science by Argonne National Laboratory under Contract No. DE-AC02-06CH11357. The XAS experiments were performed at CLAESS beamline at ALBA Synchrotron with the collaboration of ALBA staff. Authors would like to acknowledge the use of Servicio General de Apoyo a la Investigación-SAI, Universidad de Zaragoza. We would like to thank D. Haskel, M.A. Laguna, N. Menendez and A. Espinosa for assistance during experiments and S. Baker for the Fe fcc reference spectrum.

* anlaguna@unizar.es

[1] F. Wilhelm, P. Poulopoulos, H. Wende, A. Scherz, K. Baberschke, M. Angelakeris, N. K. Flevaris, and A. Rogalev, Phys. Rev. Lett. **87**, 207202 (2001).
[2] J. Balogh, , C. Fetzer, D. Kaptás, L. F. Kiss, I. S. Szücs, I. Dézsi, and I. Vincze, Phys. stat. sol. (a) **8**, 1828 (2008).
[3] Q. Zhang, P. Li, Y. Wen, C. Zhao, J. W. Zhang, A. Manchon, W. B. Mi, Y. Peng, and X. X. Zhang, Phys. Rev. B **94**, 024428 (2016).
[4] T. L. Monchesky, A. Enders, R. Urban, K. Myrtle, B. Heinrich, X.-G. Zhang, W. H. Butler, and J. Kirschner, Phys. Rev. B **71**, 214440 (2005).
[5] D. Alba-Venero, L. Fernández-Barquin, J. Alonso, M. L. Fdez-Gubieda, R. Boada, and J. Chaboy, J. Phys.: Condens. Matter **25**, 276001 (2013).
[6] J. Alonso, M. L. Fdez-Gubieda, G. Sarmiento, J. Chaboy, R. Boada, A. G. Prieto, D. Haskel, M. A. Laguna-Marco, J. C. Lang, C. Meneghini, et al., Nanotechnology **23**, 025705 (2012).
[7] Y.-S. Chen, C.-H. Lee, and H.-J. Lin, J. Vac. Sci. Technol. B **34**, 04J109 (2016).
[8] C. Chappert, A. Fert, and F. N. Van Dau, Nat Mater **6**, 813 (2007).
[9] T. Seki, Y. Hasegawa, S. Mitani, S. Takahashi, H. Imamura, S. Maekawa, J. Nitta, and K. Takanashi, Nat Mater **7**, 125 (2008).
[10] S. Hussain, C. S. Bhatia, H. Yang, and A. J. Danner, Appl. Phys. Lett. **104**, 111107 (2014).
[11] E. M. Davis, K. Zhang, Y. Cui, H. Kuhlenbeck, S. Shaikhutdinov, and H.-J. Freund, Surf. Sci. **636**, 42 (2015).
[12] R. Ramos, A. Anadón, I. Lucas, K. Uchida, P. A. Algarabel, L. Morellón, M. H. Aguirre, E. Saitoh, and M. R. Ibarra, APL Mater. **4**, 104802 (2016).
[13] Z. Ding, B. L. Chen, J. H. Liang, J. Zhu, J. X. Li, and Y. Z. Wu, Phys. Rev. B **90**, 134424 (2014).
[14] E. Snoeck, S. Frechengues, M. J. Casanove, C. Roucau, and S. Andrieu, J. Cryst. Growth **167**, 143 (1996).
[15] P. Bauer, S. Andrieu, O. M. Lemine, and M. Piecuch, J. Magn. Magn. Mater. **165**, 220 (1997).
[16] S. Andrieu, F. L. Razafindramisa, E. Snoeck, H. Renevier, A. Barbara, J. M. Tonnerre, M. Brunel, and M. Piecuch, Phys. Rev. B **52**, 9938 (1995).
[17] K. Louzazna and A. Haroun, Thin Solid Films **374**, 114 (2000).
[18] T.-H. Chuang, K. Zakeri, A. Ernst, Y. Zhang, H. J. Qin, Y. Meng, Y.-J. Chen, and J. Kirschner, Phys. Rev. B **89**, 174404 (2014).
[19] W.-H. Chen, P.-C. Jiang, C.-Y. Hsieh, and J.-S. Tsay, IEEE Trans. Magn. **50**, 2000304 (2014).
[20] D.-Y. Cho, J. Park, J. Yu, and J.-G. Park, J. Phys.: Condens. Matter **24**, 055503 (2012).
[21] A. B. Shick, S. Khmelevskyi, O. N. Mryasov, J. Wunderlich, and T. Jungwirth, Phys. Rev. B **81**, 212409 (2010).
[22] W. Witczak-Krempa, G. Chen, Y. B. Kim, and L. Balents, Annu. Rev. Condens. Matter Phys. **5**, 57 (2014).
[23] K. Fujiwara, Y. Fukuma, J. Matsuno, H. Idzuchi, Y. Niimi, Y. Otani, and H. Takagi, Nat. Commun. **4**, 2893 (2013).

[24] M. A. Laguna-Marco, J. Sanchez-Marcos, N. Menendez, J. Chaboy, E. Salas-Colera, and C. Prieto, Mater. Des. **93**, 388 (2016).
[25] C. R. Natoli, D. Misemer, S. Doniach, and F. Kutzler, Phys. Rev. A **22**, 1104 (1980).
[26] M. Benfatto and S. D. Longa, J. Synchrotron Rad. **8**, 1087 (2001).
[27] J. Chaboy and S. Quartieri, Phys. Rev. B **52**, 6349 (1995).
[28] J. Chaboy, J. Synchrotron Rad. **16**, 533 (2009).
[29] J. Chaboy, A. Muñoz-Páez, F. Carrera, P. Merkling, and E. Sánchez-Marcos, Phys. Rev. B **71**, 134208 (2005).
[30] D. E. Sayers and B. Bunker, *X-Ray Absorption: Principles, Applications, Techniques of EXAFS, SEXAFS, and XANES* (Wiley: New York, 1988), chap. 6.
[31] M. Newville, J. Synchrotron Rad. **8**, 322 (2001).
[32] B. Ravel and M. Newville, J. Synchrotron Rad. **12**, 537 (2005).
[33] R. A. Brand, Nucl. Instrum. Methods Phys. Res. B **28**, 398 (1987).
[34] See Supplemental Material at [] for further details on structural information.
[35] S. H. Baker, M. Roy, S. C. Thornton, and C. Binns, J. Phys.: Condens. Matter **24**, 176001 (2012).
[36] M. Benfatto, J. A. Solera, J. G. Ruiz, and J. Chaboy, Chemical Physics **282**, 441 (2002).
[37] C. Piquer, M. A. Laguna-Marco, A. G. Roca, R. Boada, C. Guglieri, and J. Chaboy, J. Phys. Chem. C **118**, 1332 (2014).
[38] J. P. Clancy, N. Chen, C. Y. Kim, W. F. Chen, K. W. Plumb, B. C. Jeon, T. W. Noh, and Y.-J. Kim, Phys. Rev. B **86**, 195131 (2012).
[39] F. Jimenez-Villacorta, Ph.D. thesis, Universidad Autónoma de Madrid (2007).
[40] S. Gu, W. He, M. Zhang, T. Zhuang, Y. Jin, H. ElBidweihy, Y. Mao, J. H. Dickerson, M. J. Wagner, E. D. Torre, et al., Sci. Rep. **4**, 6267 (2014).
[41] Y. Z. Wu, G. S. Dong, and X. F. Jin, Phys. Rev. B **64**, 214406 (2001).
[42] X. Yan and Y. Xu, J. Appl. Phys. **79**, 6013 (1996).
[43] J. Geshev, A. D. C. Viegas, and J. E. Schmidt, J. Appl. Phys. **84**, 1488 (1998).
[44] E. D. Torre and L. H. Bennett, J. Appl. Phys. **115**, 17A720 (2014).
[45] J. Nogués, J. Sort, V. Langlais, V. Skumryev, S. Suriñach, J. S. Muñoz, and M. D. Baró, Phys. Rep. **422**, 65 (2005).
[46] J. Sánchez-Marcos, M. A. Laguna-Marco, R. Martínez-Morillas, E. Céspedes, F. Jiménez-Villacorta, N. Menéndez, and C. Prieto, J. Phys.: Condens. Matter **23**, 476003 (2011).
[47] E. Mazario, P. Herrasti, M. P. Morales, and N. Menéndez, Nanotechnology **23**, 355708 (2012).
[48] M. Sasaki, P. E. Jönsson, H. Takayama, and H. Mamiya, Phys. Rev. B **71**, 104405 (2005).
[49] R. W. Chantrell, N. S. Walmsley, J. Gore, and M. Maylin, J. Appl. Phys. **85**, 4340 (1999).
[50] W. A. A. Macedo and W. Keune, Phys. Rev. Lett. **61**, 475 (1988).
[51] M. J. Martínez-Pérez, R. de Miguel, C. Carbonera, M. Martínez-Júlvez, A. Lostao, C. Piquer, C. Gómez-Moreno, J. Bartolomé, and F. Luis, Nanotechnology **21**, 465707 (2010).
[52] L. Rebbouh, R. P. Hermann, F.Grandjean, T. Hyeon, K. An, A. Amato, and G. J. Long, Phys. Rev. B **76**, 174422 (2007).
[53] V. V. Krishnamurthy, M. Suzuki, N. Kawamura, T. Ishikawa, and Y. Kohori, Physica B **312-313**, 647 (2002).
[54] B. T. Thole, P. Carra, F. Sette, and G. van der Laan, Phys. Rev. Lett. **68**, 1943 (1992).
[55] P. Carra, B. T. Thole, M. Altarelli, and X. Wang, Phys. Rev. Lett. **70**, 694 (1993).
[56] I. A. Campbell, J. Phys. F: Metal Phys. **2**, L47 (1972).
[57] M. A. Laguna-Marco, P. Kayser, J. A. Alonso, M. J. Martínez-Lope, M. van Veenendaal, Y. Choi, and D. Haskel, Phys. Rev. B **91**, 214433 (2015).
[58] A. Kolchinskaya, P. Komissinskiy, M. B. Yazdi, M. Vafaee, D. Mikhailova, N. Narayanan, H. Ehrenberg, F. Wilhelm, A. Rogalev, and L. Alff, Phys. Rev. B **85**, 224422 (2012).
[59] L. Zhang, Y. K. Takahashi, A. Perumal, and K. Hono, J. Magn. Magn. Mater. **322**, 2658 (2010).
[60] R. Barua, F. Jiménez-Villacorta, and L. H. Lewis, Appl. Phys. Lett. **103**, 102407 (2013).
[61] Z. Li, Y. Li, X. Liu, W. Lu, J. Bai, F. Wei, and D. Wei, IEEE Trans. Magn. **47**, 3092 (2011).